12-2015

Validation of the Global Distribution of CO_2 Volume Mixing Ratio in the Mesosphere and Lower Thermosphere from SABER

L. Rezac

Y. Jian

J. Yue

J. M. Russell III

A. Kutepov

See next page for additional authors

Original Publication Citation

Rezac, L., Jian, Y., Yue, J., Russell, J. M., III, Kutepov, A., Garcia, R., . . . Bernath, P. (2015). Validation of the global distribution of CO_2 volume mixing ratio in the mesosphere and lower thermosphere from SABER. *Journal of Geophysical Research: Atmospheres, 120*(23), 12,067-12,081. doi:10.1002/2015JD023955

AGU PUBLICATIONS

JGR

Journal of Geophysical Research: Atmospheres

RESEARCH ARTICLE
10.1002/2015JD023955

Key Points:
- Mean SABER CO_2 distribution is validated against SD-WACCM and ACE-FTS data
- SABER and ACE-FTS mean CO_2 VMR agree within 5% below 90 km up to 20% at 110 km
- SD-WACCM and SABER CO_2 spatial and seasonal distribution show a good agreement

Correspondence to:
L. Rezac,
rezac@mps.mpg.de

Citation:
Rezac, L., Y. Jian, J. Yue, J. M. Russell III, A. Kutepov, R. Garcia, K. Walker, and P. Bernath (2015), Validation of the global distribution of CO_2 volume mixing ratio in the mesosphere and lower thermosphere from SABER, *J. Geophys. Res. Atmos.*, *120*, 12,067–12,081, doi:10.1002/2015JD023955.

Received 19 JUL 2015
Accepted 20 NOV 2015
Accepted article online 23 NOV 2015
Published online 14 DEC 2015

Validation of the global distribution of CO_2 volume mixing ratio in the mesosphere and lower thermosphere from SABER

L. Rezac[1,2], Y. Jian[2], J. Yue[2], J. M. Russell III[2], A. Kutepov[3,4], R. Garcia[5], K. Walker[6], and P. Bernath[7]

[1]Max-Planck-Institut für Sonnensystemforschung, Göttingen, Germany, [2]Center for Atmospheric Sciences, Hampton University, Hampton, Virginia, USA, [3]NASA Goddard Space Flight Center, Greenbelt, Maryland, USA, [4]Physics Department, The Catholic University of America, Washington, District of Columbia, USA, [5]Atmospheric Chemistry Division, National Center for Atmospheric Research, Boulder, Colorado, USA, [6]Department of Physics, University of Toronto, Toronto, Ontario, Canada, [7]Department of Chemistry and Biochemistry, Old Dominion University, Norfolk, Virginia, USA

Abstract The Sounding of the Atmosphere using Broadband Emission Radiometry (SABER) instrument on board the Thermosphere Ionosphere Mesosphere Energetics and Dynamics satellite has been measuring the limb radiance in 10 broadband infrared channels over the altitude range from ~ 400 km to the Earth's surface since 2002. The kinetic temperatures and CO_2 volume mixing ratios (VMRs) in the mesosphere and lower thermosphere have been simultaneously retrieved using SABER limb radiances at 15 and 4.3 μm under nonlocal thermodynamic equilibrium (non-LTE) conditions. This paper presents results of a validation study of the SABER CO_2 VMRs obtained with a two-channel, self-consistent temperature/CO_2 retrieval algorithm. Results are based on comparisons with coincident CO_2 measurements made by the Atmospheric Chemistry Experiment Fourier transform spectrometer (ACE-FTS) and simulations using the Specified Dynamics version of the Whole Atmosphere Community Climate Model (SD-WACCM). The SABER CO_2 VMRs are in agreement with ACE-FTS observations within reported systematic uncertainties from 65 to 110 km. The annual average SABER CO_2 VMR falls off from a well-mixed value above ~80 km. Latitudinal and seasonal variations of CO_2 VMRs are substantial. SABER observations and the SD-WACCM simulations are in overall agreement for CO_2 seasonal variations, as well as global distributions in the mesosphere and lower thermosphere. Not surprisingly, the CO_2 seasonal variation is shown to be driven by the general circulation, converging in the summer polar mesopause region and diverging in the winter polar mesopause region.

1. Introduction

Carbon dioxide (CO_2) is an important greenhouse gas in Earth's atmosphere because it is transparent to incoming visible solar light but absorbs outgoing infrared radiation. Observations show that the tropospheric CO_2 concentration has been increasing at a rate of 1–2 parts per million by volume (ppmv) per year since 1960 [*Tans and Keeling*, 2014], which is mostly attributed to fossil fuel burning and deforestation. There is a time lag of about 5 years for changes in tropospheric air to reach the middle and upper atmosphere through transport [*Bischof et al.,* 1985], where the continual rise of the CO_2 concentration is expected to significantly influence the thermal structure [*Roble and Dickinson*, 1989; *Akmaev*, 2002; *Garcia et al.,* 2007]. Due to rising CO_2 levels, the upper atmosphere, unlike the lower atmosphere, is predicted to experience strong cooling and contraction, which may have significant consequences for low Earth orbit spacecraft [e.g., *Lewis et al.,* 2011; *Emmert et al.,* 2012]. CO_2 also plays an important role as a tracer of turbulent mixing that defines the height of the turbopause [*Garcia et al.,* 2014]. In addition, knowledge of vertical profiles of CO_2 volume mixing ratio (VMR) in the upper atmosphere is required for interpretation of satellite observations of infrared radiation of CO_2 bands used to retrieve kinetic temperature and other chemical constituents [*Lopez-Puertas et al.,* 2000; *Remsberg et al.,* 2008].

The first direct measurements of CO_2 in the mesosphere and lower thermosphere (MLT) were provided by rocket-borne mass spectrometers [*Offermann and Grossmann*, 1973; *Philibrick et al.,* 1973; *Trinks and Fricke*, 1978; *Offermann et al.,* 1981]. These data show a nearly constant CO_2 VMR up to ~90–100 km altitude. However, rocket measurements only take place in limited regions and special times. Global monitoring of CO_2 concentration can only be carried out by spaceborne instruments measuring either atmospheric emission or absorption of CO_2 bands [*Lopez-Puertas et al.,* 2000]. The advantage of the satellite solar occultation remote sensing technique is that absorption is a much more direct measurement of the CO_2 ground-state

density, which is only weakly affected by nonlocal thermodynamic equilibrium (non-LTE) effects. However, only ~30 solar occultation profiles per day are collected from sunset and sunrise measurements for an instrument in a typical low Earth orbit. Occultation measurements of CO_2 density in the mesosphere and lower thermosphere (MLT) have been made by several spaceborne experiments including the Grille spectrometer on board Spacelab 1 [*Girard et al.,* 1988], the Atmospheric Trace Molecule Spectroscopy interferometer on Spacelab 3 [*Rinsland et al.,* 1992], and during the Atmospheric Laboratory for Applications and Science 1, 2, and 3 missions [*Kale and Miller*, 1996]. These measurements showed CO_2 to be well mixed up to 90 km altitude. A recent solar occultation experiment, the Atmospheric Chemistry Experiment Fourier transform spectrometer (ACE-FTS) on board SCISAT [*Bernath et al.,* 2005], showed latitudinal variability of the departure of CO_2 VMR from the well-mixed value, which on average occurred at a lower altitude (~80 km) than previously found [*Beagley et al.,* 2010].

The CO_2 limb emissions can also be used to retrieve CO_2 VMRs but with a broader daily global coverage than the occultation measurements. However, the retrieval algorithm is more complicated due to non-LTE effects in the molecular energy levels from which the emissions originate [*Lopez-Puertas et al.,* 2000]. Emissions from the $CO_2(\nu_3)$ band at 4.3 μm or the $CO_2(\nu_2)$ band at 15 μm were obtained from rocket-borne spectrometer measurements made during the Spectral Infrared Rocket Experiment [*Wintersteiner et al.,* 1992; *Nebel et al.,* 1994] and the Spectroscopic Infrared Structure Signatures Investigation [*Vollmann and Grossmann*, 1997] and from satellite measurements made by the Stratospheric and Mesospheric Sounder on Nimbus 7 [*Lopez-Puertas and Taylor*, 1989], and its successor, the Improved Stratospheric and Mesospheric Sounder on the Upper Atmosphere Research Satellite [*Lopez-Puertas et al.,* 1998; *Zaragoza et al.,* 2000]. These measurements covered altitude ranges between 60 and 120 km. The Cryogenic Infrared Spectrometers and Telescopes for the Atmosphere (CRISTA) experiment, on board the Space Shuttle mission in November 1994 and August 1997, also provided global CO_2 measurements in the altitude range 60–130 km [*Offermann et al.,* 1999; *Kaufmann et al.,* 2002]. These measurements, (CRISTA), sampled a latitude range of 60°N–60°S with a mean CO_2 VMR profile departing from a well-mixed value at ~70 km. Summaries of past CO_2 observations are provided in a review paper by *Lopez-Puertas et al.* [2000] and also in *Kaufmann et al.* [2002] and *Beagley et al.* [2010].

The main processes controlling the annual mean vertical distribution of the CO_2 VMR below about 10^{-4} hPa (~105–110 km) are eddy diffusion and molecular diffusive separation; above that altitude, photolytic and other loss mechanisms of CO_2, as well as molecular diffusion, become increasingly important [*Garcia et al.,* 2014]. The interplay of eddy diffusion and molecular diffusive separation strongly influences the altitude where the CO_2 VMR departs from the well-mixed value. Photolysis is found to play a minor role in governing the CO_2 VMR below 110 km. *Garcia et al.* [2014] provide an updated review of these processes and show the calculated CO_2 and CO height distributions using the Specified Dynamics version of the Whole Atmosphere Community Climate Model (SD-WACCM) constrained by Modern-Era Retrospective Analysis for Research and Applications (MERRA) data below about 1 hPa (50 km).

In this paper we report on the validation of global CO_2 VMR data obtained from a self-consistent two-channel inversion of the Sounding of the Atmosphere using Broadband Emission Radiometry (SABER) v2.0 4.3 μm and 15 μm radiances. The two-channel retrieval algorithm is described in detail in *Rezac et al.* [2015]. The retrievals are performed on postprocessed radiances, meaning radiances for which pressure and altitude registration, spacecraft motion effects, and other radiance correction factors that must be done before retrievals started have already been implemented by the SABER operational processing code. This paper is structured in the following way: the SABER and ACE-FTS instruments and the coincident observations are described in section 2. A summary of the SABER two-channel retrieval algorithm and its associated uncertainties are discussed in section 3. In section 4, the coincident SABER and ACE-FTS CO_2 VMR profiles are compared, along with the comparisons of the SABER CO_2 VMR altitude, latitude, and seasonal distributions with the SD-WACCM simulations. In section 5, a summary of the main results and conclusions are presented.

2. The SABER and ACE-FTS CO_2 Observations

The SABER instrument on Thermosphere Ionosphere Mesosphere Energetics and Dynamics was launched on 7 December 2001, and it has become one of the longest (13 years since 2002) operating infrared sensors,

providing about 1400 profiles a day with nearly global coverage. The SABER limb scans provide simultaneous radiance profiles in 10 spectral channels over the range 1.27–17 μm. The SABER channels include CO_2 emission bands at both 4.3 μm and 15 μm, with a field of view of 2 km that is oversampled with vertical steps of 0.375 km. The horizontal resolution is dictated by the limb geometry and is ~300 km. The latitude coverage is 82°N–53°S or 53°N–82°S, with alternating coverage due to the spacecraft 60 day yaw cycle. A detailed description of the SABER instrument and data retrieval, in particular the operational temperature results, can be found in *Russell et al.* [1999] and *Remsberg et al.* [2008], respectively.

The ACE-FTS mounted on the SCISAT platform was launched into a 74° inclination circular orbit at an altitude of 650 km on 12 August 2003. The ACE-FTS is a high spectral resolution (0.02 cm^{-1}) Fourier transform spectrometer operating in the 750–4400 cm^{-1} (2.2–13.3 μm) range. Using solar occultation, the ACE-FTS measures limb infrared absorption spectra, which are then translated into transmittances using exo-atmospheric observations. Each day, it is possible to obtain a maximum of about 15 sunrise profiles and 15 sunset profiles. Thus, there are a total of ~30 vertical occultation scans per day [*Bernath et al.,* 2005]. For this work, version 3.0 ACE-FTS retrievals are used [*Boone et al.,* 2013]. Vertical profiles of temperature and CO_2 densities are obtained in the MLT from a total of 67 microwindows in the spectral ranges of 4.82–5.26 μm and 4.18–4.36 μm [*Beagley et al.,* 2010]. Because of the relationship between T_k and CO_2 number density, the simultaneous retrieval is a strongly ill-posed problem; and in the absence of additional constraints, the inversion may yield unphysical oscillations in the vertical profiles. Therefore, the ACE-FTS CO_2 VMR profile is parameterized in the 60–120 km altitude range, and only the appropriate coefficients are retrieved through least squares fitting. The estimated vertical resolution is between 2 and 6 km depending on the beta angle of the orbit (i.e., the angle between the orbital plane and the satellite-Sun vector).

3. SABER Self-Consistent T_k/CO_2 Two-Channel Retrieval Algorithm

The v2.0 SABER measured limb radiances at 4.3 μm and 15 μm are used to simultaneously obtain vertical profiles of kinetic temperature, T_k, and CO_2 VMR. In the current stage, the two-channel algorithm is applied only for SABER daytime observations for solar zenith angles $<80°$ (this is done to achieve better signal-to-noise ratio). We are currently revisiting the nighttime 4.3 μm forward model in order to apply the same methodology to obtain T_k/CO_2 at night in the near future. Additional screening based on the *Kp* index < 4 is applied in order to sample only geomagnetically quiet conditions (to avoid the possibility of significant NO^+ emission into the SABER 4.3 μm channel). In the MLT the SABER measured limb emissions are significantly influenced by non-LTE conditions. The fundamental band at 15 μm starts deviating from LTE near 80 km, and sometimes even lower, depending on the actual temperature profile [*Garcia-Comas et al.,* 2008], while the 4.3 μm levels are already in non-LTE as low as 50–55 km altitude during daytime. The mechanisms involved in the non-LTE populations of the CO_2 vibrational levels are summarized in more detail by *Lopez-Puertas and Taylor* [2001]. As already noted, the two-channel inversion is applied to postoperationally processed data in which the CO_2 vibrational populations along with the forward modeling of non-LTE limb radiances are calculated with the accelerated lambda iteration for atmospheric radiation and molecular spectra package [*Kutepov et al.,* 1998; *Gusev and Kutepov*, 2003; *Rezac et al.,* 2015] based on the Accelerated Lambda Iteration approach [*Rybicki and Hummer*, 1991].

The two-channel self-consistent T_k/CO_2 inversion is achieved by iterating over two independent relaxation modules, one for T_k and one for the CO_2 VMR. The current approach is selected from several inversion techniques mainly for its speed, stability, and flexibility, and it builds upon a similar approach used in the v1.06 SABER data inversion [*Mertens et al.,* 2003]. The algorithm uses modified Chahine profile update functions [*Chahine*, 1972; *Twomey et al.,* 1977] for both T_k and CO_2 VMR, with additional control to ensure a similar relaxation speed for both channels [*Rezac et al.,* 2015]. A detailed error analysis was performed, which reveals that the T_k and CO_2 VMR profile uncertainties are dominated by systematic errors. The largest uncertainty is attributed to non-LTE modeling parameters, such as collisional rate coefficients, and also to the assumed density of the collisional partners, such as atomic [O] and [$O(^1D)$] above 90 km. Table 1 summarizes the error budget of the daytime retrieved CO_2 VMR under non-LTE conditions representative of an instantaneous profile. The individual errors, as well as the total error (root-sum-square, or RSS), are detailed for six altitude regions in the MLT. The error analysis was carried out by simulating measured radiance for nominal atmospheric and forward model input values. The individual parameters were then perturbed one at a time, and the two-channel inversion algorithm was iterated until convergence. The mean error was calculated

Table 1. Two-Channel CO_2 VMR Retrieval Errors (%) and Their Sources[a]

	Altitude (km)				
Error Source[b]	70	80	90	100	110
Random noise[c]	-		±1	±1	±2
Radiance bias[d]	-	-	±1	±2	±1
$P(z=0)$ bias	-		±4	±4	±3
$T(z)$ bias	-	-	±6	±6	±4
Atomic O bias	-		±2	±7	±13
$O(^1D)$ bias	-	-	±5	±14	±23
Kvv N_2-$O(^1D)$	-	-	±3	±9	±11
Kvt CO_2-O	-	-	±1	±2	±5
Kvt $CO_2(\upsilon_3 - \upsilon_2)$[e]	-	-	±3	±3	±4
Kvv CO_2-N_2	-	-	±6	±3	±10
Root-sum-square	±15	±15	±12	±21	±32

[a] CO_2 VMR retrieved at altitudes between 110 and 130 km relies on the WACCM inputs. While these are consistent with each other, the parameters such as O and $O(^1D)$ are not known very accurately. For these reason, the error may be in fact larger than indicated (assumed accuracy of 50%).
[b] CO_2 VMR in (%).
[c] SABER noise equivalent radiance values.
[d] Reference pressure at 30 km.
[e] Splitting of CO_2 υ_3 quanta into 1–4 (υ_2) quanta in *V-T* collisions with N_2.

for four different input atmospheric conditions. The individual error sources below 90 km altitude are given only as a total RSS, because the SABER CO_2 VMR profile is constrained to not exceed 15% of the constant value below 65 km. The complete details of all the individual error sources are presented in *Rezac et al.* [2015].

The inversion is applied in the altitude ranges 65–110 km and 65–130 km for T_k and CO_2 VMR, respectively. Therefore, the actual self-consistent two-channel retrieval applies only in the altitude range 65–110 km. The retrieved T_k and CO_2 VMR values at the lower boundary are constrained to smoothly join the SABER operationally retrieved temperatures (http://saber.gats-inc.com/) and the WACCM CO_2 VMR profile, while at the upper boundary they join with the WACCM supplied T_k and CO_2 VMR profiles (for more details, see *Rezac et al.* [2015]). The SABER operational T_k retrieval is performed using the so-called interleaving process, where essentially five separate retrievals are performed on a 2 km vertical grid spacing with each one shifted by 0.375 km (vertical scan sampling resolution). After convergence, these five retrievals are then averaged together to obtain a single profile with about 2 km vertical resolution [*Remsberg et al.,* 2008]. In the case of the two-channel inversion, only a single retrieval is made on a uniform 1 km altitude grid. Due to the nature of the two-channel inverse

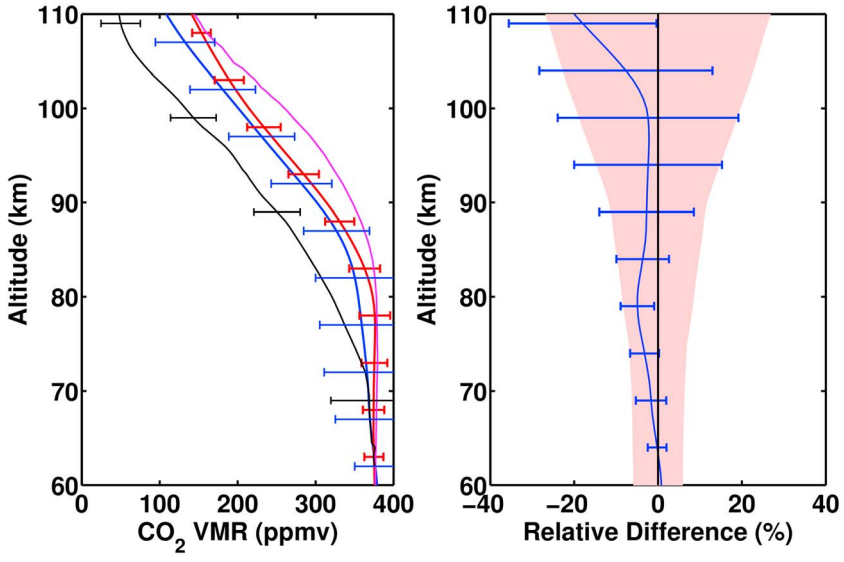

Figure 1. (left) Comparison of mean CO_2 VMR profiles between SABER (blue line) and ACE-FTS (red line) assembled from 9 years of coincident measurements as discussed in the text. Mean CO_2 VMR profiles from CRISTA-1 [*Kaufmann et al.,* 2002] (black line) and the Rocket measurements [*Wintersteiner et al.,* 1992] (magenta line) are shown for comparison. The uncertainties for each instrument are indicated by the error bars at the selected altitudes. All profiles are scaled to the same value at 60 km. (right) The mean relative difference between coincident SABER and ACE-FTS CO_2 pairs is plotted as the blue curve on the right, and the error bars indicate the standard deviation of the difference. The combined uncertainty of SABER and ACE is indicated in shaded area. CRISTA-1 profile is scaled to match the SABER CO_2 at 60 km.

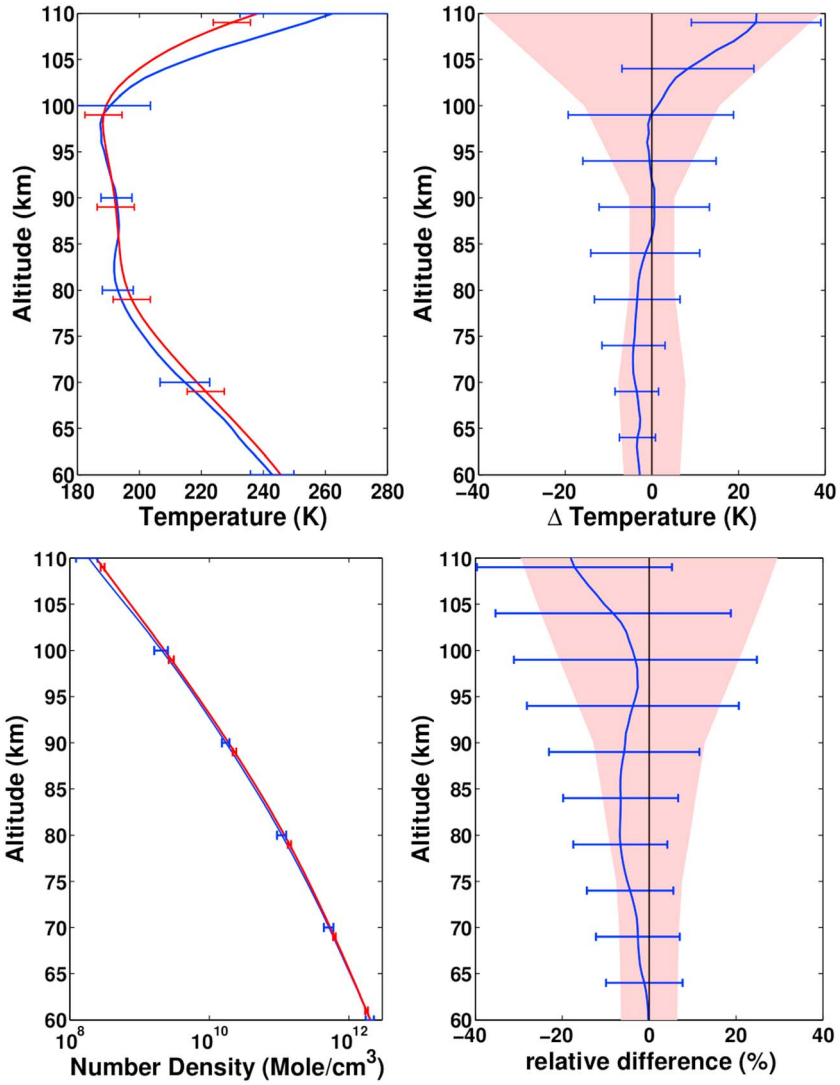

Figure 2. (top left) Comparison of mean SABER (blue line) and mean ACE-FTS (red line) kinetic temperature profiles for all coincident pairs along with the standard deviation of the mean (shown as error bars). (top right) Mean of the temperature differences (SABER-ACE-FTS) shown as the blue curve with the standard deviation of the mean shown as error bars. The combined uncertainty of SABER and ACE-FTS is indicated in the shaded area. (bottom left) Comparison of mean SABER (blue line) and mean ACE-FTS (red line) CO_2 number density measurements with standard deviation of the mean as error bars selected at several altitudes. (bottom right) Mean relative difference between the two data sets (blue curve) with the standard deviation (blue error bars). The shaded area, as before, shows the combined uncertainty of the CO_2 number density.

problem under non-LTE, and partly because of the applied smoothing regularization during the relaxation iteration (2 km sliding boxcar window), the vertical resolution of the T_k profiles is 3–6 km depending on how many iterations the inversion takes. In general, it takes more iterations to reach convergence under cold summer mesopause conditions. The non-LTE effects are very strong in the 4.3 μm emissions (starting below 65 km), which leads to additional degradation of the vertical resolution of the CO_2 VMR due to photon scattering in the 65–80 km region**.** The typical vertical resolution for CO_2 VMR varies between 4 and 12 km, depending on the season, and better resolution (4–6 km) is generally achieved during the equinoxes. In the summer high latitudes below 90 km, the vertical resolution is lost completely, because the SABER observations are constrained to retrieve a mean value in the range (65–90 km). The mean is assigned to a (average) grid point at 77 km with a line fit in between the end points (for detailed reasoning and discussion, see *Rezac et al.* [2015]).

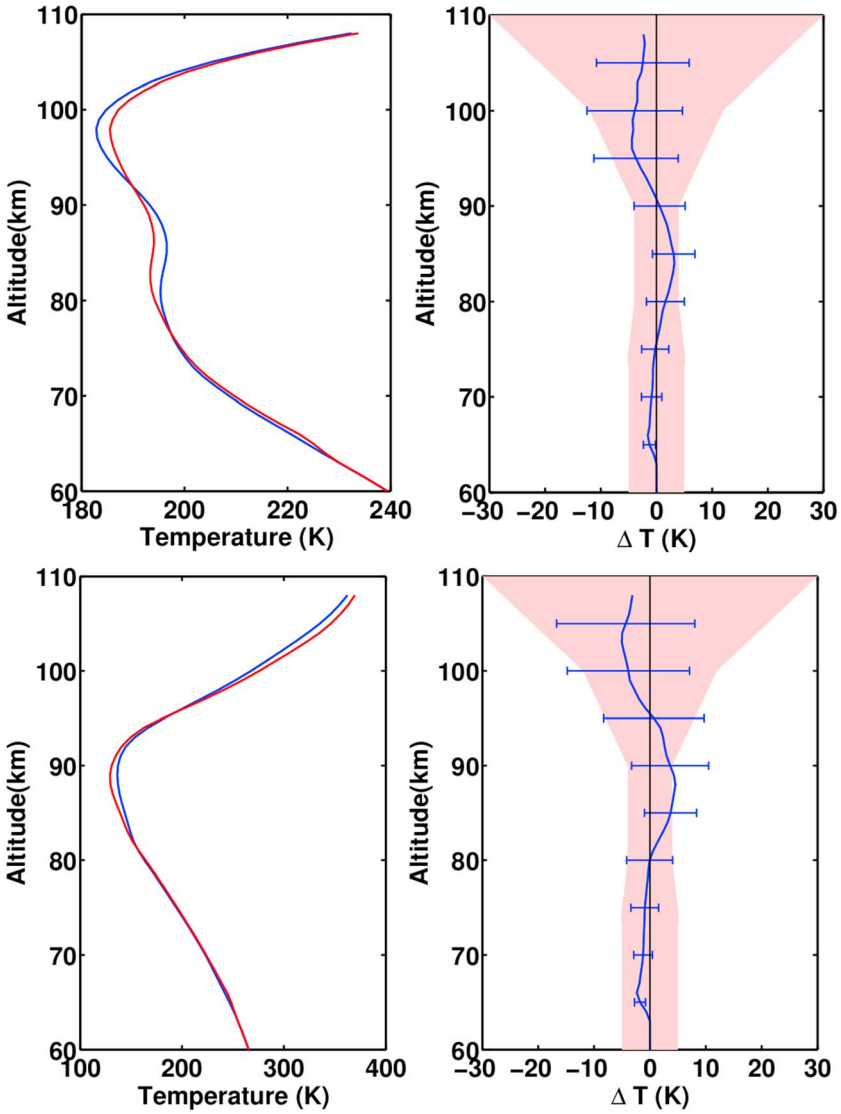

Figure 3. (top left) Comparison of the March and September mean vertical profile from SABER operationally retrieved v2.0 kinetic temperature (blue line) and the simultaneously retrieved SABER T_k/CO_2 kinetic temperature (red line). (bottom left) The same comparison as before but for the January and July mean summer hemisphere (see text). (right column) The associated mean differences are in blue color with the standard deviation of the differences indicated as error bars. The combined uncertainty of the two retrievals is shown as a shaded area in Figure 3 (right column).

4. SABER CO_2 Validation Studies

4.1. Comparison With Coincident ACE-FTS Data

The SABER CO_2 data for 2004–2012 are first compared with coincident ACE-FTS version 3.0 observations. We have applied a screening process to the ACE-FTS database to discard bad data in the same way as was done by *Garcia et al.* [2014]. The distribution of CO_2 in the MLT (below about 10^{-4} hPa) is mainly controlled by eddy diffusion and molecular diffusive separation instead of photolysis [*Garcia et al.,* 2014]. Thus, a wider range of coincidence criteria can be applied compared to that of temperature (±5° for latitude, ±10° for longitude, and ±4 h for time), similar to the approach used by *Rong et al.* [2009] for SABER ozone validation.

The majority of coincident pairs occur in the latitude ranges of ±50 to ±80° in the equinox months. Among the total of 943 coincident pairs, about 800 pairs occur in March and about 100 pairs occur in September, with more than 650 pairs occurring between the latitudes 70–80°. This is a direct result of the spatial sampling of ACE-FTS observations that are optimized for measurements in the polar regions.

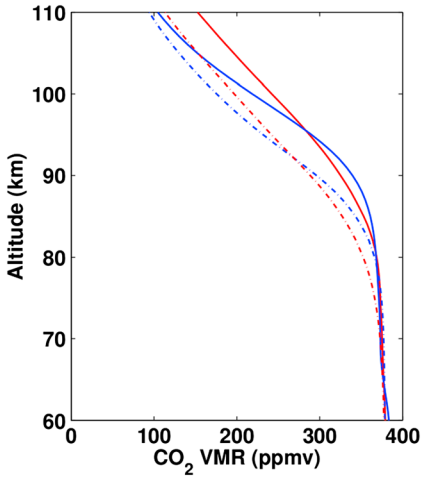

Figure 4. Global mean CO_2 VMR profiles for 2004 to 2012 from SABER (full blue) and ACE-FTS (full red). Two SD-WACCM mean CO_2 VMR profiles are also shown as dash-dotted lines. The SD-WACCM results correspond to the weighted average taking into account the space time sampling of the zonal means by the instrument. WACCM data corresponding to the sampling of SABER and ACE-FTS data are shown by the dash-dotted blue curve and the dash-dotted red curve, respectively. See detailed discussion in the text.

Independent measurements in the past decade have shown that CO_2 above about 80 km is not uniformly mixed but exhibits considerable temporal and spatial variability. In Figure 1, mean CO_2 VMR profiles obtained from CRISTA-1 and mean rocket measurements [*Wintersteiner et al.,* 1992] are plotted for qualitative comparison with the ACE-FTS and SABER. Figure 1 (left column) shows the comparison of mean profiles including all the coincident SABER and ACE-FTS CO_2 VMR data in the 9 year period 2004–2012 with the total (random and systematic) uncertainties shown as error bars. The ACE-FTS data have been interpolated onto a 1 km grid, which is used in SABER postoperational processing retrievals. Both the ACE-FTS and SABER CO_2 VMR profiles show a rapid decrease above ~80 km (defined as the "knee" of the profile). The SABER CO_2 profile has the same slope (~10 ppmv/km) as the ACE-FTS profile above ~85 km. Above ~100 km, these two profiles diverge from each other with the mean ACE-FTS CO_2 VMR being generally greater than the SABER VMR. Nevertheless, the mean profiles are within the estimated uncertainties of each other nearly over the entire altitude range up to 100 km. The estimated vertical resolution of SABER is very similar to that of ACE-FTS (about 4–5 km) in these coincident profile comparisons which apply to the equinox season. No additional measures for possibly different averaging kernels (AKs) between the instruments were taken into account in these comparisons. Since neither SABER nor ACE-FTS inversion calculations provide routine AKs for the converged solution, it is not possible to account for inverse process smoothing of the true profile as proposed by *Rodgers and Connor* [2003]. In order to display statistically sound comparisons, we plot the total combined error of SABER and ACE-FTS as a shaded region in the figures. The error bars include the effects of smoothing of the true profiles by the inversion (by virtue of how the errors are estimated, see *Rezac et al.* [2015]). The CRISTA-1 observations shown in Figure 1 were obtained in November 1994 and covered a latitude range from 52°S to 63°N [*Kaufmann et al.,* 2002]. The global mean CRISTA-1 CO_2 profile starts departing from a well-mixed value at ~72 km, which is much lower than SABER and ACE-FTS, as well as the rocket measurement. Figure 1 (right column) shows the relative difference between the SABER and ACE-FTS measurements. Here the relative difference is defined as $(VMR_{SABER}\text{-}VMR_{ACE})/VMR_{ACE}$, and the total error is defined as the root-sum-square of uncertainties of both the SABER CO_2 and ACE-FTS CO_2 VMR. [*Beagley et al.,* 2010]. The SABER CO_2 VMR is systematically slightly lower than the ACE-FTS VMR over the entire MLT. The relative differences are smaller than 5% below 100 km; above ~100 km the differences increase significantly and reach ~20% at 110 km. The standard deviation of the relative differences shown as the error bars (on the blue curve) is still within the combined systematic uncertainties of the two measurements.

Both SABER and ACE-FTS obtain CO_2 VMR and temperature simultaneously in the range 65–110 km. Therefore, comparing CO_2 number density is also highly desirable, as this quantity is of direct interest for photochemical models. Figure 2 shows a comparison of the kinetic temperature and CO_2 number density from coincident SABER and ACE-FTS measurements. *Beagley et al.* [2010] estimate the uncertainties of ACE-FTS temperature as a constant 6 K for altitudes above 60 km, while the detailed temperature uncertainty for the SABER 2-channel inversion is detailed as a function of altitude in *Rezac et al.* [2015]. The combined uncertainties are denoted by pink shading in Figure 2 (right column). The mean of the temperature difference between SABER and ACE-FTS is smaller than 4 K below 85 km, which is consistent with the validation results of *Sica et al.* [2008], although their work focused on the region below 70 km and they used an early version of SABER temperature. From 85 km to 100 km, the two data sets match very well, although their variance is relatively large.

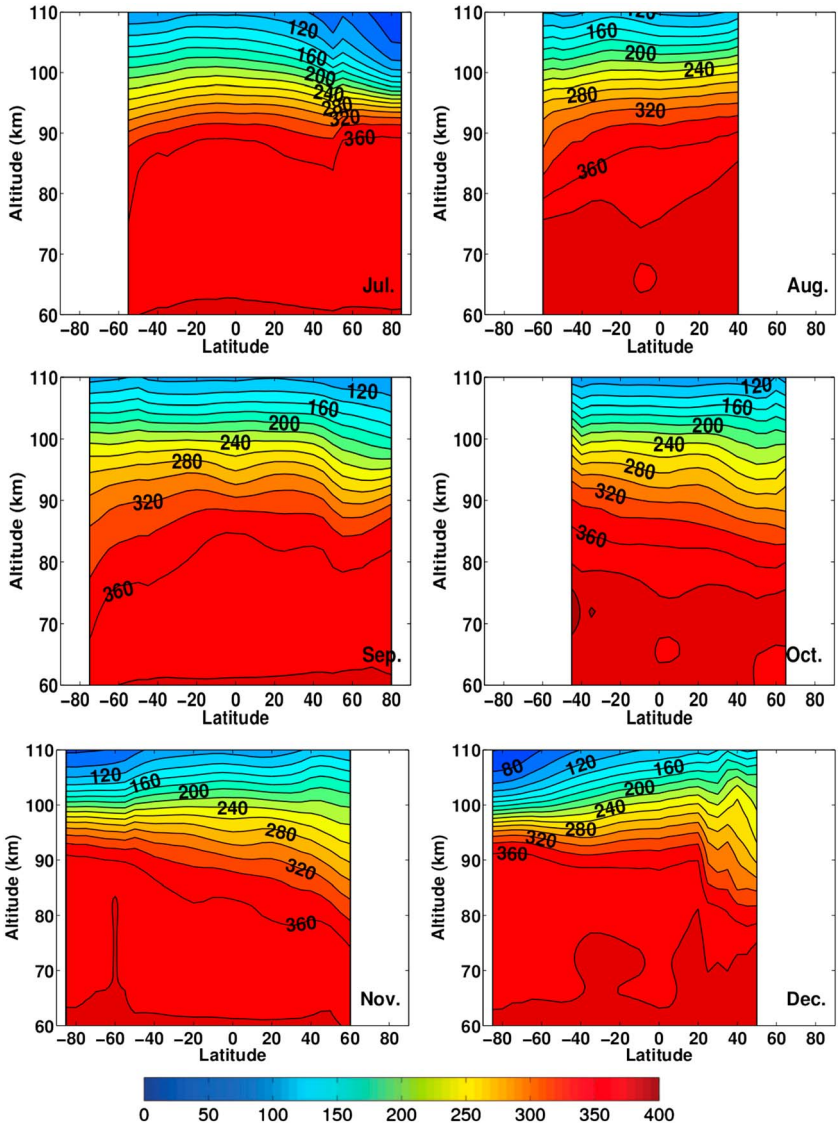

Figure 5. (a) Monthly zonal mean SABER CO_2 VMR (ppmv) altitude versus latitude cross sections for January through June averaged over the 9 year period from 2004 to 2012. (b) Same as Figure 5a but for the period July through December.

Currently, the operational SABER v2.0 kinetic temperature retrieval uses the CO_2 VMR from WACCM similar to the v1.07 retrieved temperature profiles [*Remsberg et al.,* 2008]. As indicated earlier, the simultaneously retrieved T_k/CO_2 data obtained in a postprocessing mode are publicly available on the SABER website. The comparison between SABER v2.0 temperature and simultaneously retrieved T_k/CO_2 at the equinox (March and September, combined) and summer (Northern Hemisphere in July and Southern Hemisphere in January, combined) for high latitudes (±50–82°) is shown in Figure 3. The simultaneously retrieved T_k is ~5 K colder than SABER v2 temperature at 80–95 km in the summer polar region. The difference between these two SABER temperature results above 100 km is comparable to the measurement uncertainties (>10 K). (Additional details on the two SABER T_k data sets and their uncertainties are provided at the SABER website: http://saber.gats-inc.com/temp_errors.php).

4.2. Comparison Between SABER CO_2 and the SD-WACCM Simulations

As an upper atmosphere extension of the Community Atmosphere Model, WACCM has been used to study the chemistry, radiation, and dynamics in the middle and upper atmosphere and their impact on the Earth's climate [*Smith et al.,* 2011]. This model extends from the surface to the thermosphere (~5.96×10^{-6} hPa or ~ 140 km).

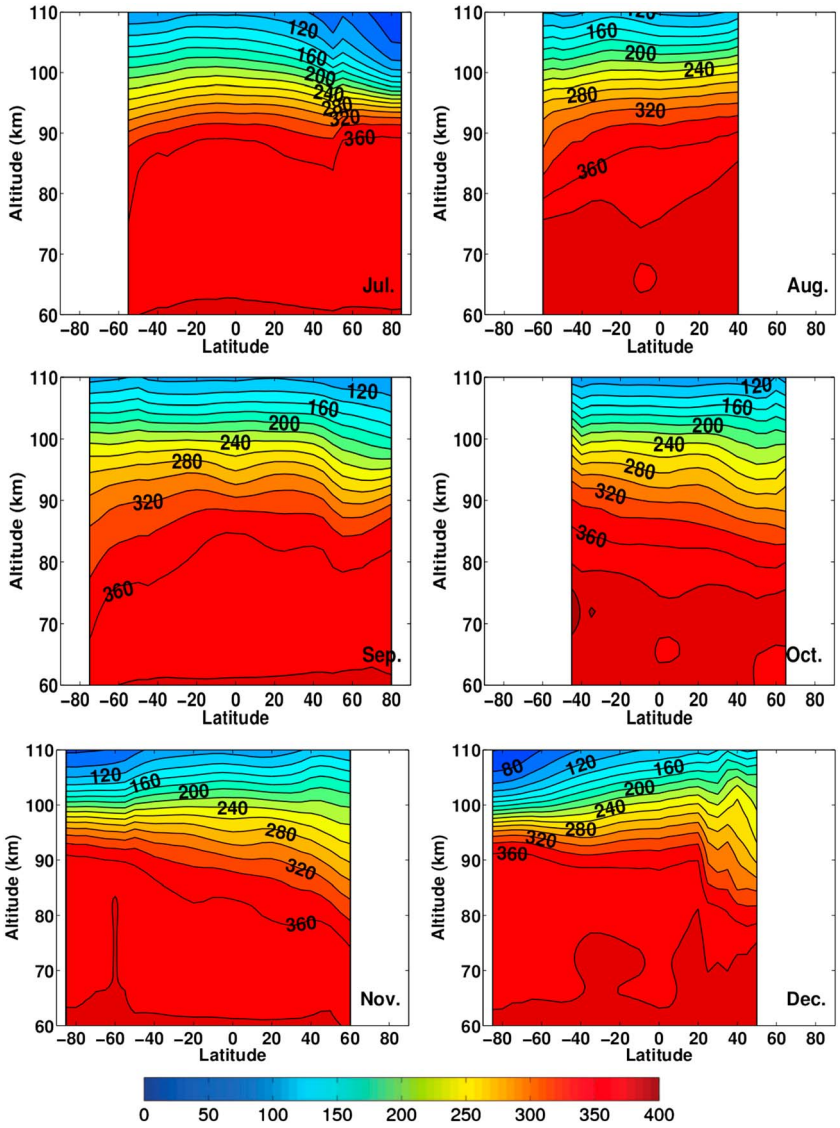

Figure 5. (continued)

A detailed description of WACCM v4 is given by *Marsh et al.* [2013]. *Garcia et al.* [2007] showed that the temperature and zonal winds in WACCM are consistent with global satellite observations. *Smith et al.* [2011] used WACCM to study the relationship between the transformed Eulerian mean (TEM) circulation and the distribution of CO_2 in the MLT. In this paper, output from the specified dynamics version of the model, SD-WACCM, for the period from 2003 to 2012 is used. The dynamics and temperature in the troposphere and stratosphere in SD-WACCM are constrained by data from NASA's Modern-Era Retrospective Analysis for Research and Applications (MERRA) [*Rienecker et al.,* 2011]; therefore, the dynamics in SD-WACCM follows MERRA observations in the altitude range where MERRA data are available over this period. The model transitions to free running above about 1 hPa.

These model results compared here were obtained with a Prandtl number of 4, which is the standard setting in WACCM4. The Prandtl number, Pr, is the ratio of momentum diffusivity to thermal diffusivity and may be considered a tunable parameter in the gravity wave parameterization used in WACCM. Recently, *Garcia et al.* [2014] showed that using Pr = 2 could give better agreement between the CO_2 VMR calculated with WACCM and ACE-FTS measurements than Pr = 4. The smaller Pr leads to a larger eddy diffusion coefficient, which increases the VMR of CO_2 above 80 km. They also showed that realistic CO could be obtained concurrently if all known sources of CO from CO_2 were included in the calculation and a relatively small value for the cross section of O_2 was used in the frequency band 105–121 nm. Notwithstanding, the specification of additional

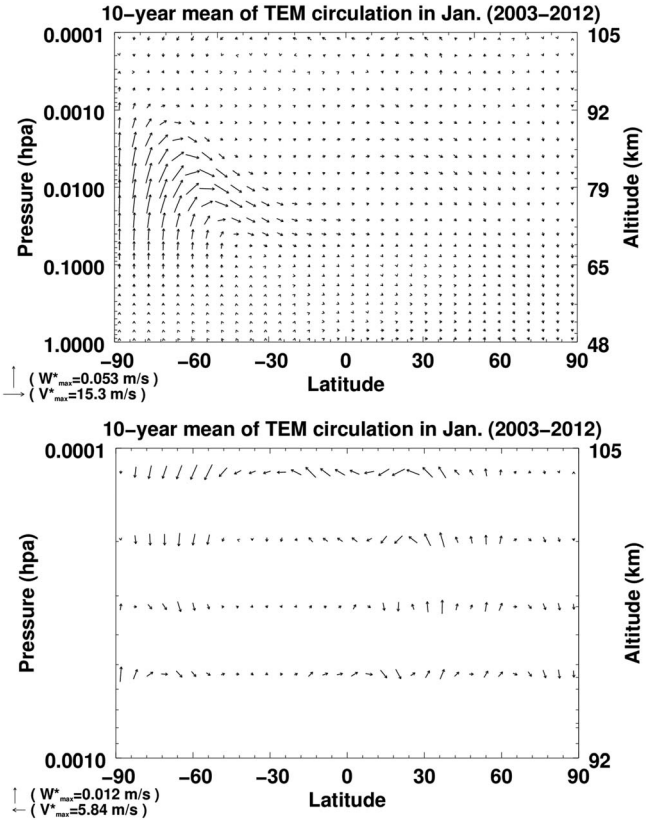

Figure 6. Nine year (2004–2012) zonal mean SD-WACCM transformed Eulerian circulation shown for January. (top) A global view of the TEM circulation pattern. (bottom) A zoomed-in view to better illustrate the reversal of the TEM meridional circulation above 90–95 km (see text for details).

loss mechanisms for CO_2, the vertical profile of the latter was affected relatively little because photolytic loss is not a major component of the CO_2 budget below 10^{-4} hPa.

Figure 4 shows the profiles of global annual mean CO_2 VMR profiles from SABER, ACE-FTS measurements, and the SD-WACCM simulation. Unlike the SD-WACCM output, the spatial and temporal sampling of ACE-FTS data are quite inhomogeneous, and while SABER data are sampled much more uniformly, they are obtained only for daytime in the case of CO_2. For this reason the two SD-WACCM profiles in Figure 4 are weighted means with the number of profiles available in a given month and latitude bin for SABER and ACE-FTS as the weights. The effect of the seasonal variability and general circulation is largely removed in the annual, global means, while only eddy diffusion and molecular diffusion determine the shapes of the profiles. It is obvious that the WACCM CO_2 falls off from its well-mixed state at lower altitudes (~5 km) compared to ACE-FTS and SABER. This may be taken to imply an underestimation of vertical eddy diffusion in SD-WACCM with the standard setting, Pr = 4. The effects of increasing the eddy mixing by reducing the Pr number result in a better match of the model with the measurements, as noted above and discussed by *Garcia et al.* [2014].

The 9 year (2004–2012) zonally averaged SABER CO_2 VMR distribution for each month is shown in Figure 5. We note that, because of the long duration of the SABER data set and its broad spatial and temporal coverage, the cross section of monthly CO_2 VMR is unprecedentedly complete despite the fact that SABER CO_2 VMR is obtained only during daytime. The main features revealed by the SABER CO_2 VMR zonal mean distributions are (1) notable seasonal variability at high latitudes, (2) very rapid decrease of the CO_2 VMR above 90 km in polar summer, (3) early departure from a well-mixed CO_2 profile during the equinoxes, especially at high latitudes (usually around 75–80 km), and (4) generally lower CO_2 VMR around 110 km altitude during equinox seasons compared to solstice. It is clear that CO_2 isolines in the MLT are relatively close together at summer high latitudes and farther apart in the winter polar region, as in the WACCM simulation discussed by *Smith et al.* [2011]. To relate the CO_2 distribution to the general circulation, Figure 6 illustrates the SD-WACCM TEM meridional and vertical wind vector for January (solstice). The TEM during solstice shows two circulation patterns in two layers. Below about 90 km, there is upwelling in summer and downwelling in winter; above 90 km, the opposite pattern appears, with upwelling in winter and downwelling in summer. As discussed in *Smith et al.* [2011], the different patterns of the residual circulation below and above 90 km are induced by a change of sign in the zonal mean zonal force due to breaking gravity waves. Since CO_2 has a long enough lifetime to be a tracer on a seasonal time scale, convergence in the winter causes a higher concentration of CO_2 while divergence has the opposite effect, consistent with the SABER observations shown in Figure 5.

Most coincident SABER and ACE-FTS measurements occur in March and September and within latitude bands of ±50 to ±80°. Consequently, the coincident pair comparisons in Figure 1 may not reflect accurately the

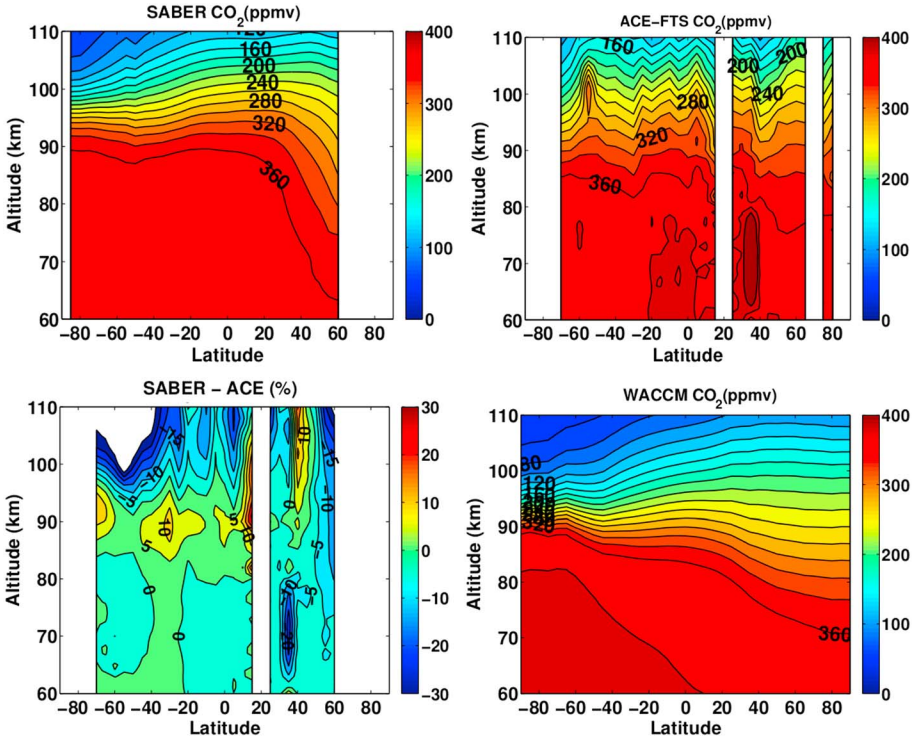

Figure 7. (top left) January zonal mean SABER CO_2 VMR (ppmv) altitude versus latitude cross section over the 9 year period from 2004 to 2012. (top right). Same as Figure 7 (top left) except for ACE-FTS. (bottom left) Cross section of the mean relative difference (%) between SABER and ACE-FTS, and (bottom right) January zonal mean SD-WACCM CO_2 (ppmv) altitude versus latitude cross section over the same 9 year period.

mean averaged over the different seasons. Therefore, the zonal mean distribution of CO_2 VMR from SABER, ACE-FTS observations, and SD-WACCM simulations as a function of latitude and altitude are compared in Figures 7–10.

The SD-WACCM simulations indicate that, during solstice, due to the upward transport in the summer hemisphere and downward transport in the winter hemisphere below 90 km, the CO_2 VMR remains constant up to higher altitudes in the summer hemisphere and departs from its well-mixed value at lower altitudes in the winter hemisphere. This pattern is shown in the WACCM cross sections in Figures 7 and 8. The altitude of constant SABER CO_2 VMR remains at 90 km from the southern polar region to 20°N, then decreases very rapidly with increasing latitude, while the altitude of constant CO_2 VMR in WACCM decreases gradually from the south polar region. Thus, in the northern polar region below about 95 km, the vertical gradient of SABER CO_2 is considerably smaller than the vertical gradient from the WACCM simulation. On the other hand, the summer to winter slope of the CO_2 distribution is not obvious in the ACE-FTS CO_2 cross section. As a consequence, above 100 km, the ACE-FTS CO_2 VMR in the summer polar region is much higher than the SABER measurements and the WACCM simulation. Also, the meridional distribution of ACE-FTS CO_2 is not as "smooth" as the other two CO_2 data sets, presumably due to the sparseness of ACE-FTS measurements. Below 95 km, the magnitude of the relative difference between SABER and ACE-FTS CO_2 is less than 10% except near 30°N, where the ACE-FTS CO_2 VMR reaches 400 ppmv, which is likely an outlier, as such a value was not reached in troposphere during the period investigated here. Above 95 km, the difference gradually increases to 25%, except in the summer polar region. This is consistent with the coincident measurement comparison.

In the summer season there is a notable discontinuity (an increase or a decrease in VMR depending on the hemisphere) in SABER CO_2 near 50°, as shown in Figure 5, while the WACCM CO_2 distributions are quite smooth. This feature is a result of a local SABER time sampling bias arising from using only the daytime measurements in the current CO_2 retrievals. At latitudes poleward of 50° only local morning/evening atmospheric conditions are probed (see Figure 1 in *Rezac et al.* [2015]), which in turn leads to a bias in the typical pressure profiles compared to the scenario where we average morning and afternoon data together. This ultimately

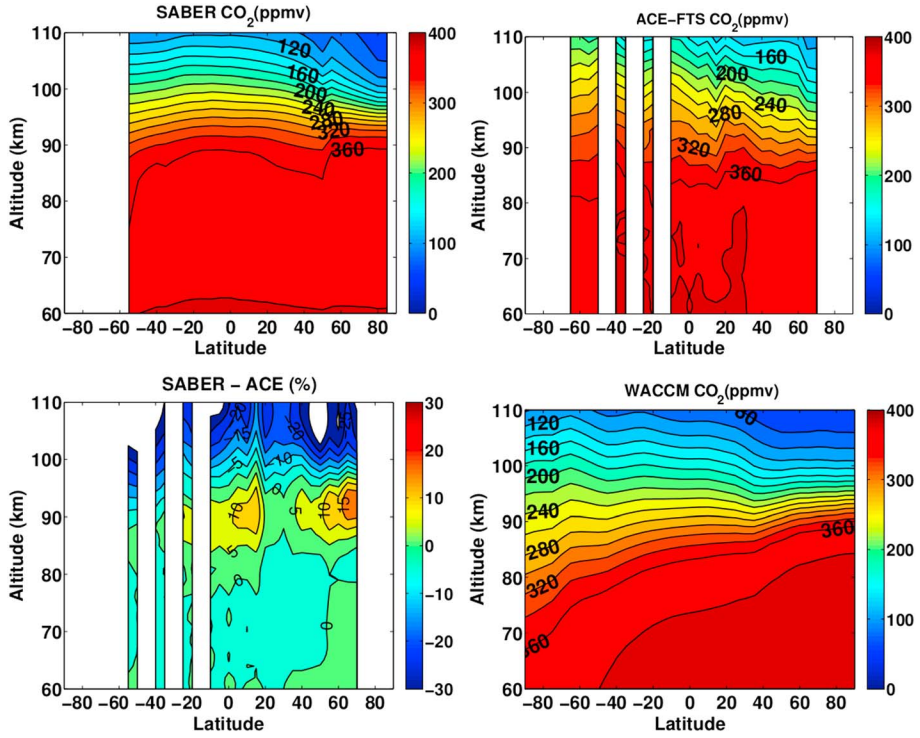

Figure 8. Same as Figure 7 but for July.

results in a noticeable drop or increase (depending on the hemisphere) in the SABER CO_2 VMR. As the measurement point moves toward the poles, at around 60–70°, polar day conditions with a constant 24 h illumination are encountered, where the temperatures are higher again starting from the lower stratosphere to the lower mesosphere (15–60 km), which affects the lower atmospheric pressure. This feature can also be clearly seen in the pressure distribution between the morning and evening local times at 35 km (figure not shown). The origin of this anomaly is therefore clear and removes any questions about it being an artifact of influence from above such as NO^+ and/or aurora effects on CO_2 emissions.

The convergence of CO_2 in the polar regions (south in March and north in September) is not present in the equinox months, since the meridional circulation is much different from the solstice conditions. The SABER CO_2 distributions match the WACCM CO_2 better in equinox seasons than in solstice months, as shown in Figures 9 and 10. Above 90 km, the WACCM CO_2 distribution has a wavy shape, i.e., there are maxima at midlatitudes and minima at the equator and in the polar regions. This wavy feature reflects the WACCM TEM circulation pattern at high altitudes, converging and sinking at the equator, diverging and rising at midlatitudes (not shown). This wavy feature can also be seen in the SABER CO_2 distribution, although the magnitude is much weaker than that in SD-WACCM. As in the solstice months, except in the region 0–20°N above 90 km, the SABER CO_2 VMR is smaller than the ACE-FTS CO_2 VMR near the equinox. As the altitude increases, the magnitude of the relative difference increases gradually, though the magnitude ($<$25%) is not as large as in the solstice months ($>$30%). In general, it should be kept in mind that the current SABER CO_2 data are collected only for daytime conditions, and the effects of tides, at low latitude to midlatitude, could be present in the zonal mean cross sections especially during the equinox seasons.

5. Conclusions

Comparison of SABER CO_2 VMR over the 65–110 km range with coincident ACE-FTS measurements indicates that these two data sets provide consistent results in terms of the vertical shape of the profiles. Although the SABER CO_2 measurement is systematically lower than the ACE-FTS in the MLT, the discrepancy is within the uncertainties of each data set. From 65 to ~100 km, the mean difference between the two data sets is smaller

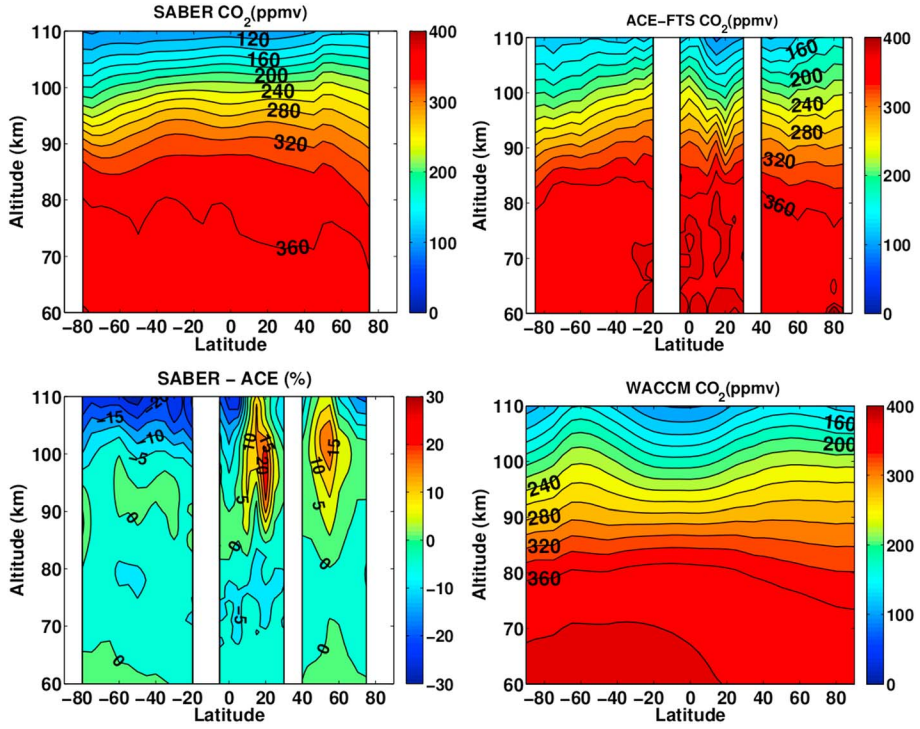

Figure 9. Same as Figure 7 but for March.

than 5% but it increases to 20% at 110 km. Even at the 1σ level, the difference is still smaller than the combined uncertainties of the two data sets. The comparison of kinetic temperature and CO_2 number density yields a similar result with the differences being within the combined error of the two retrievals. However, the CO_2 number density differences are slightly larger than CO_2 VMR differences between SABER and ACE-FTS.

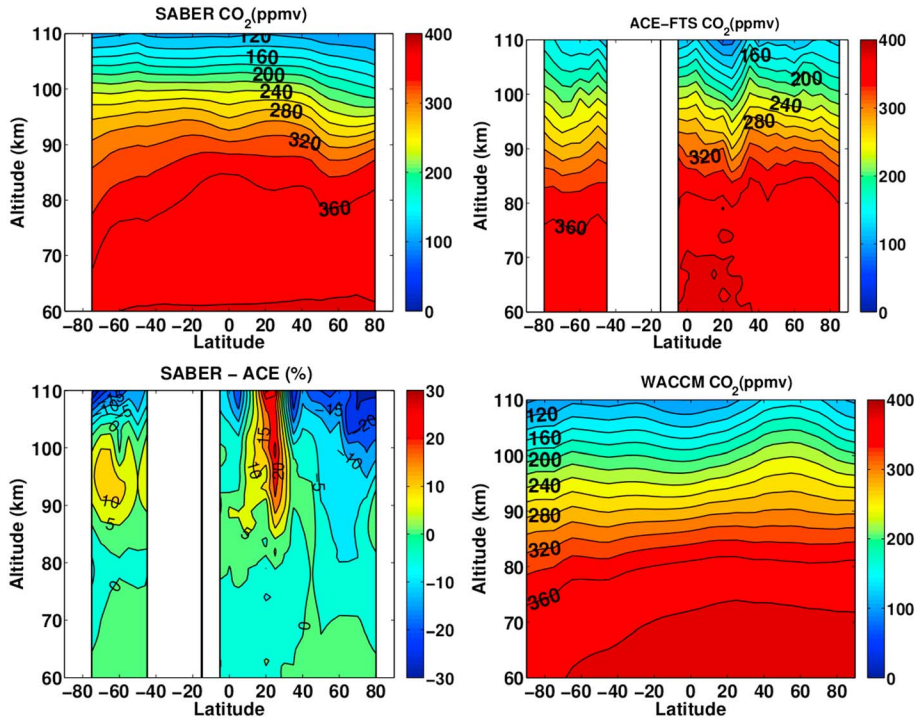

Figure 10. Same as Figure 7 but for September.

We also investigated the mean differences between the SABER operationally retrieved temperatures and the two-channel retrieved temperatures self-consistently obtained with the CO_2 VMR. The comparison between SABER operational v2.0 kinetic temperature and the temperature from the simultaneous T_k/CO_2 retrievals indicates that during the solstice months in the polar regions the mean difference is >5 K at 85–90 km (operational T_k is higher). Nevertheless, the differences are within the combined measurement uncertainties.

Altitude versus latitude cross sections of monthly and zonal mean CO_2 VMRs from SABER measurements and SD-WACCM simulations show overall agreement in terms of the seasonal variation and vertical distribution throughout the mesosphere and lower thermosphere. Both data sets show that the strongest vertical gradient of CO_2 occurs above the polar summer mesopause. Examination of the mean meridional circulation in WACCM suggests that this behavior is due the fact that the meridional circulation in the lower thermosphere reverses relative to its counterpart in the mesosphere at about 90–95 km (cf. Figure 6). The behavior of the general circulation toward the winter hemisphere is also well captured by the SABER CO_2 VMR distribution, demonstrating the seasonal variations. We note that some of these features cannot be found in the ACE-FTS monthly zonal mean observations because of the sparse temporal and spatial coverage.

Acknowledgments

We would like to acknowledge the hard work and support of the SABER retrieval team who provided the version 2.0 data, including scientists from GATS, Inc, NASA Langley Research Center, NASA Goddard Space Flight Center, Spain (IAA), and Arcon, Inc. The SABER experiment and retrieval work are supported by NASA grant NNX11AD63G. The ACE mission is supported primarily by the Canadian Space Agency. The National Center for Atmospheric Research is supported by the U.S. National Science Foundation. L.R. acknowledges funding from NASA grant NNX11AD63G. J.Y. is supported by NASA grants NNX14AF20G and NNH13ZDA001N-HGI. A.K. was supported by NASA grant NNX11AM24G. We are grateful to Martin Kaufmann for providing the CRISTA CO_2 profiles. The new v2.0 SABER products as well as the simultaneously retrieved T_k/CO_2 presented in this paper are accessible from the SABER website: http://saber.gats-inc.com/data.php. We thank the two anonymous reviewers for their constructive comments, which improved this manuscript.

References

Akmaev, R. A. (2002), Modeling the cooling due to CO2 increases in the mesosphere and lower thermosphere, *Phys. Chem. Earth*, *27*, 521–528.

Beagley, S. R., C. D. Boone, V. I. Fomichev, J. J. Jin, K. Semeniuk, J. C. McConnell, and P. F. Bernath (2010), First multi-year occultation observation of CO_2 in the MLT by ACE satellite: Observation and analysis using the extended CMAM, *Atmos. Chem. Phys.*, *10*, 1133–1153.

Bernath, P. F., et al. (2005), Atmospheric Chemistry Experiment (ACE): Mission overview, *Geophys. Res. Lett.*, *32*, L15S01, doi:10.1029/2005GL022386.

Bischof, W., R. Borchers, P. Fabian, and B. C. Kruger (1985), Increased concentration and vertical distribution of carbon dioxide in the stratosphere, *Nature*, *316*, 708–710.

Boone, C., K. Walker, and K. Walker (2013), Version 3 retrievals for the atmospheric chemistry experiment Fourier transform spectrometer (ACE-FTS), in *The Atmospheric Chemistry Experiment ACE at 10: A Solar Occultation Anthology*, edited by P. Bernath, pp. 103–127, A. Deepak Publ., Hampton, Va.

Chahine, M. T. (1972), A general relaxation method for inverse solution of full radiative transfer equation, *J. Atmos. Sci.*, *29*, 513–518.

Emmert, J. T., M. H. Stevens, P. F. Bernath, D. P. Drob, and C. D. Boone (2012), Observations of increasing carbon dioxide concentration in Earth's thermosphere, *Nat. Geosci.*, *5*, 868–871, doi:10.1038/NGEO1626.

Garcia, R. R., D. R. Marsh, D. E. Kinnison, B. A. Bovill, and F. Sassi (2007), Simulation of secular trends in the middle atmosphere, 1950–2003, *J. Geophys. Res.*, *112*, D09301, doi:10.1029/2006JD007485.

Garcia, R. R., M. Lopez-Puertas, B. Funke, D. R. Marsh, D. E. Kinnison, and A. K. Smith (2014), On the distribution of CO_2 and CO in the mesosphere and thermosphere, *J. Geophys. Res. Atmos.*, *119*, 5700–5718, doi:10.1002/2013JD021208.

Garcia-Comas, M., et al. (2008), Error in sounding of the atmosphere using broadband emission radiometry (SABER) kinetic temperature caused by non-local thermodynamic equilibrium model parameters, *J. Geophys. Res.*, *113*, D24106, doi:10.1029/2008JD010105.

Girard, A., J. Besson, D. Brard, J. Laurent, M. P. Lemaitre, C. Lippens, C. Muller, J. Vercheval, and M. Ackerman (1988), Global results of Grille spectrometer experiment on board Spacelab 1, *Planet Space Sci.*, *36*, 291–300.

Gusev, O. A., and A. A. Kutepov (2003), Non-LTE gas in planetary atmospheres, *ASP Conf. Ser.*, *228*, 318–330.

Kale, J. A., and T. L. Miller (1996), The ATLAS series of shuttle missions, *Geophys. Res. Lett.*, *23*, 2285–2288.

Kaufmann, M., O. A. Gusev, K. U. Grossmann, R. G. Roble, M. E. Hagan, C. Hartsough, and A. A. Kutepov (2002), The vertical and horizontal distribution of CO_2 densities in the upper mesosphere and lower thermosphere as measured by CRISTA, *J. Geophys. Res.*, *107*(D23), 8182, doi:10.1029/2001JD000704.

Kutepov, A. A., O. A. Gusev, and V. P. Ogibalov (1998), Solution of the non-LTE problem for molecular gas in planetary atmospheres: Superiority of accelerated lambda iteration, *J. Quant. Spectros. Radiat. Transfer*, *60*, 199–220.

Lewis, H. G., A. Saunders, G. Swinerd, and R. J. Newland (2011), Effect of thermospheric contraction on remediation of the near-Earth space debris environment, *J. Geophys. Res.*, *116*, A00H03, doi:10.1029/2011JA016482.

Lopez-Puertas, M., and F. W. Taylor (1989), Carbon dioxide 4.3 μm emission in the Earth's atmosphere: A comparison between NIMBUS 7 SAMS measurements and non-local thermodynamic equilibrium radiative transfer calculation, *J. Geophys. Res.*, *94*, 13,045–13,068.

Lopez-Puertas, M., and F. W. Taylor (2001), *Non-LTE Radiative Transfer in the Atmosphere*, *Ser. Atmos. Oceanic Planet. Phys.*, vol. 3, World Sci.

Lopez-Puertas, M., M. G. Zaragoza, and M. A. Lopez-Valverde (1998), Non local thermodynamic equilibrium (LTE) atmospheric limb emission at 4.6 μm, an analysis of the daytime wideband radiance as measured by UARS improved stratospheric and mesospheric sounder, *J. Geophys. Res.*, *103*, 8515–8530.

Lopez-Puertas, M., M. A. Lopez-Valverde, R. R. Garcia, and R. G. Roble (2000), A review of CO_2 and CO abundance in the middle atmosphere, *Geophys. Monogr.*, *123*, 83–100.

Marsh, D. R., M. E. Mills, D. E. Kinnison, J.-F. Lamarque, N. Calvo, and L. M. Polvani (2013), Climate change from 1850 to 2005 simulated in CESM1 (WACCM), *J. Clim.*, *26*, 7372–7391, doi:10.1175/JCLI-D-12-0558.1.

Mertens, C. J., M. G. Mlynczak, M. López-Puertas, P. P. Wintersteiner, R. H. Picard, J. R. Winick, L. L. Gordley, and J. M. Russell III (2003), Retrieval of the kinetic temperature and carbon dioxide abundance from non-local thermodynamic equilibrium limb emission measurements made by the SABER experiment on the TIMED satellite, *SPIE Proc. Remote Sens. Clouds Atmos. VII*, *4882*, 162–171, doi:10.1117/12.463358.

Nebel, H., P. P. Wintersteiner, R. H. Picard, J. R. Winick, and R. D. Sharma (1994), CO_2 non-local thermodynamic equilibrium radiative excitation and infrared dayglow at 4.3 μm: Application to Spectral Infrared Rocket Experiment data, *J. Geophys. Res.*, *99*(D5), 10,409–10,419.

Offermann, D., and K. U. Grossmann (1973), Thermospheric density and compositions as determined by a mass spectrometer with cryo ion source, *J. Geophys. Res.*, *78*, 8296–8304.

Offermann, D., V. Friedrich, P. Ross, and U. von Zahn (1981), Neutral gas composition measurements between 80 and 120 km, *Planet. Space Sci.*, *29*(7), 747–764, doi:10.1016/0032-0633(81)90046-5.

Offermann, D., K.-U. Grossmann, P. Barthol, P. Knieling, M. Riese, and R. Trant (1999), Cryogenic Infrared Spectrometers and Telescopes for the Atmosphere (CRISTA) experiment and middle atmosphere variability, *J. Geophys. Res.*, *104*(D13), 16,311–16,325, doi:10.1029/1998JD100047.

Philibrick, C. R., G. A. Faucher, and E. Trzcinski (1973), Rocket measurements of mesospheric and lower thermospheric composition, *Space Res.*, *13*, 255–260.

Remsberg, E. E., et al. (2008), Assessment of the quality of the version 1.07 temperature-versus pressure profiles of the middle atmosphere from TIMED/SABER, *J. Geophys. Res.*, *113*, D17101, doi:10.1029/2008JD010013.

Rezac, L., A. Kutepov, J. M. Russell III, A. G. Feofilov, and J. Yue (2015), Simultaneous retrieval of T(p) and CO_2 VMR for non-LTE limb radiance measured by the SABER/TIMED instrument, *J. Atmos. Solar Terr. Phys.*, *130*, 23–42, doi:10.1016/j.jastp.2015.05.004.

Rienecker, M. M., et al. (2011), MERRA: NASA's Modern-Era Retrospective Analysis for Research and Applications, *J. Clim.*, *24*, 3624–3648, doi:10.1175/JCLI-D-11-00015.1.

Rinsland, C., M. R. Gunson, R. Zander, and M. López-Puertas (1992), Middle and upper atmosphere pressure-temperature profiles and abundances of CO_2 and CO in the upper atmosphere from ATMOS/Spacelab 3 observations, *J. Geophys. Res.*, *97*, 20,479–20,495.

Roble, R. G., and R. E. Dickinson (1989), How will changes in carbon dioxide and methane modify the mean structure of the mesosphere and thermosphere?, *Geophys. Res. Lett.*, *16*, 1144–1441.

Rodgers, C. D., and B. J. Connor (2003), Intercomparison of remote sounding instruments, *J. Geophys. Res.*, *108*(D3), 4116, doi:10.1029/2002JD002299.

Rong, P., J. M. Russell III, M. G. Mlynczak, E. E. Remsberg, B. T. Marshall, L. L. Gordley, and M. López-Puertas (2009), Validation of thermosphere ionosphere mesosphere energetics and dynamics/sounding of the atmosphere using broadband emission radiometry (TIMED/SABER) v1.07 ozone at 9.6 μm in altitude range 15–70 km, *J. Geophys. Res.*, *114*, D04306, doi:10.1029/2008JD010073.

Russell, J. M., III, M. G. Mlynczak, L. L. Gordley, J. J. Tansock Jr., and R. W. Esplin (1999), Overview of the SABER experiment and preliminary calibration results, *SPIE Proc.*, *3756*, 277–288, doi:10.1117/12.366382.

Rybicki, G. B., and D. G. Hummer (1991), An accelerated lambda iteration method for multilevel radiative transfer. I. Non-overlapping lines with background continuum, *Astron. Atrophys.*, *245*, 171–181.

Sica, R. J., et al. (2008), Validation of the atmospheric chemistry experiment (ACE) version 2.2 temperature using ground-based and space-borne measurements, *Atmos. Chem. Phys.*, *8*, 35–62.

Smith, A. K., R. R. Garcia, D. R. Marsh, and J. H. Richter (2011), WACCM simulations of the mean circulation and trace species transport in the winter mesosphere, *J. Geophys. Res.*, *116*, D20115, doi:10.1029/2011JD016083.

Tans, P., and R. Keeling (2014), Trends in atmospheric carbon dioxide. [Available at http://www.esrl.noaa.gov/gmd/ccgg/trends/.]

Trinks, H., and K. H. Fricke (1978), Carbon dioxide in the lower thermosphere, *J. Geophys. Res.*, *83*, 3883–3886.

Twomey, S., B. Herman, and R. Rabinoff (1977), An extension to the Chahine method of inverting the radiative transfer equation, *J. Atmos. Sci.*, *34*, 1085.

Vollmann, K., and K. U. Grossmann (1997), Excitation of 4.3 μm CO_2 emission by O during twilight, *Adv. Space Res.*, *20*, 1185–1189.

Wintersteiner, P. P., R. H. Picard, R. D. Sharma, J. R. Winick, and R. A. Joseph (1992), Line-by-line radiative excitation model for the non-equilibrium atmosphere: Application to CO_2 15 μm emission, *J. Geophys. Res.*, *97*, 18,083–18,117.

Zaragoza, G. M., M. Lopez-Puertas, M. A. Lopez-Valverde, and F. W. Taylor (2000), Global distribution of CO_2 in the upper mesosphere as derived from UARS/ISAMS measurements, *J. Geophys. Res.*, *105*, 19,829–19,839.